

Pirin is an iron-dependent redox regulator of NF- κ B

Fange Liu^{a,b}, Imran Rehmani^a, Shingo Esaki^a, Rong Fu^{a,1}, Lirong Chen^a, Vesna de Serrano^{a,2}, and Aimin Liu^{a,b,3}

^aDepartment of Chemistry and ^bCenter for Diagnostics and Therapeutics, Georgia State University, Atlanta, GA 30303

Edited by Chuan He, University of Chicago, Chicago, IL, and accepted by the Editorial Board April 19, 2013 (received for review December 12, 2012)

Pirin is a nuclear nonheme Fe protein of unknown function present in all human tissues. Here we describe that pirin may act as a redox sensor for the nuclear factor κ B (NF- κ B) transcription factor, a critical mediator of intracellular signaling that has been linked to cellular responses to proinflammatory signals and controls the expression of a vast array of genes involved in immune and stress responses. Pirin's regulatory effect was tested with several metals and at different oxidation states, and our spectroscopic results show that only the ferric form of pirin substantially facilitates binding of NF- κ B proteins to target κ B genes, a finding that suggests that pirin performs a redox-sensing role in NF- κ B regulation. The molecular mechanism of such a metal identity- and redox state-dependent regulation is revealed by our structural studies of pirin. The ferrous and ferric pirin proteins differ only by one electron, yet they have distinct conformations. The Fe center is shown to play an allosteric role on an R-shaped surface area that has two distinct conformations based on the identity and the formal redox state of the metal. We show that the R-shaped area composes the interface for pirin-NF- κ B binding that is responsible for modulation of NF- κ B's DNA-binding properties. The nonheme Fe protein pirin is proposed to serve as a reversible functional switch that enables NF- κ B to respond to changes in the redox levels of the cell nucleus.

metalloprotein | coregulator | reactive oxygen species (ROS) | oxidative stress | signal transduction activation

The transcription factor, nuclear factor κ B (NF- κ B), discovered in 1986 (1, 2), is a ubiquitous cellular regulator widely recognized as a critical mediator of intracellular signaling for immune/inflammatory response including oxidative stress (3–5). NF- κ B is a family of structurally related and functionally conserved dimeric proteins that consist of RelA (p65), RelB, c-Rel, p50, and p52. All members can form both homo- and heterodimers with different physiological functions and gene targets (6–8). NF- κ B proteins bind and activate several hundred κ B genes in response to activating stimuli (9–11). The activity of NF- κ B is tightly controlled by regulatory proteins and cofactors collectively known as coregulators (12, 13). Complex regulatory networks exist to ensure that NF- κ B is activated only by appropriate stimuli and is then inactivated when no longer needed (14–16). NF- κ B typically resides in the cytoplasm in an apparently inhibited state, bound with an inhibitory protein known as I κ B α . Previous studies have established that NF- κ B activation is first achieved by phosphorylation of the inhibitory protein I κ B α to liberate NF- κ B proteins to their free forms. Next, NF- κ B proteins are translocated to the nucleus where, with the help of coregulators, they will orchestrate the cascade of signaling responses to the external stimuli. At present, the precise roles played by the coregulators in the cell nucleus are poorly understood.

Winnacker and coworkers in 1997 identified a highly conserved human protein by using nuclear factor I as a “bait protein” and named it pirin (17). This previously unknown protein is expressed in all human tissues. Biochemical data suggest that pirin is a nuclear protein composed of 290 aa, *ca.* 32 kDa (17). Experiments using genomic Southern and Western blots have demonstrated the presence of pirin genes and their expression in dot-like subnuclear structures that represent loci of specific nuclear processes, including DNA replication and/or RNA polymerase II transcription (17). Pirin has been found to form tight complexes with the inducible antiapoptotic transcription factor NF- κ B p50 homodimer and the B-cell lymphoma 3-encoded protein Bcl-3 (18). In a gel

mobility shift assay using cell lysates, pirin was shown to enhance the DNA-binding activity of the p50–Bcl-3 complex (18). These observations led to the initial suggestion that pirin functions as a coregulator in the NF- κ B transcription complex (18). However, such a proposed regulation has not been confirmed and the mechanism of it is completely unknown.

In the subsequent studies by various laboratories, pirin was found to be a nonheme iron-binding protein that belongs to an ancient redox-sensitive subclass of proteins in the cupin superfamily (19–21). Pirin has additionally been linked to the metastasis of melanoma cells (22, 23). It has been shown that pirin expression is significantly up-regulated in the spleen and kidney of cytosolic superoxide dismutase (SOD)-deficient mice (24). Similarly, up-regulation of *pirin* expression by chronic cigarette smoking has been associated with bronchial epithelial cell apoptosis (25). The crystal structure of pirin at 2.1-Å resolution reveals a ferrous site that is octahedrally coordinated with three histidines, one glutamate, and two water molecules (19). In the present work, we describe that pirin substantially facilitates the DNA binding of NF- κ B p65 to the I κ B gene when the metal center is a ferric ion. An unprecedented redox regulation mechanism is proposed from the previous studies and the results are described below.

Results

Human Pirin Facilitates the DNA Binding of p65 to the κ B Gene in a Redox-State-Dependent Manner. We studied the effect of pirin on the binding affinity of p65 (residues 21–325) (26) homodimers to the I κ B target sequence (I κ B) by testing isolated protein, using surface plasmon resonance (SPR) spectroscopy. The first significant observation is that Fe(III)-pirin, generated by oxidizing Fe(II)-pirin with ferricyanide, or O₂ in a relatively slower oxidation process, and verified by electronic paramagnetic resonance (EPR) spectroscopy substantially enhanced p65 binding to the I κ B target site (Fig. 1A). In the presence of 0–25 μ M Fe(III)-pirin, the binding was a two-phase process: a fast phase in the first 60 s with k_{on1} = 1.1×10^6 M⁻¹·s⁻¹ and a slow association phase after 60 s with k_{on2} = 0.02 M⁻¹·s⁻¹. The buffer rinse resulted in the loss of only a small amount of mass presumably due to washing away of nonspecifically bound proteins observed in the slower binding phase. The binding is very tight, with virtually no dissociation after removing nonspecifically bound proteins. This is unique experimental evidence of pirin interacting with p65 and dramatically enhancing the binding affinity for p65 to the κ B site. In contrast, Fe(II)-pirin does not affect p65 binding to the I κ B site. The dose response with the truncated p65 is shown in Fig. 1B. The sequence specificity of pirin's effect on p65 was further

Author contributions: F.L. and A.L. designed research; F.L., I.R., S.E., R.F., L.C., and V.d.S. performed research; S.E. performed site-directed mutagenesis analyses; F.L., I.R., R.F., V.d.S., and A.L. analyzed data; and F.L., I.R., and A.L. wrote the paper.

The authors declare no conflict of interest.

This article is a PNAS Direct Submission. C.H. is a guest editor invited by the Editorial Board.

Data deposition: The atomic coordinates and structure factors have been deposited in the Protein Data Bank, www.pdb.org (PDB ID codes 4GUL, 4EWA, 4EWE, 4ERO, 4EWD, and 4HLT).

¹Present address: Department of Neurology, Emory University, Atlanta, GA 30322.

²Present address: School of Medicine, University of Maryland, Baltimore, MD 21201.

³To whom correspondence should be addressed. E-mail: feradical@gsu.edu.

This article contains supporting information online at www.pnas.org/lookup/suppl/doi:10.1073/pnas.1221743110/-DCSupplemental.

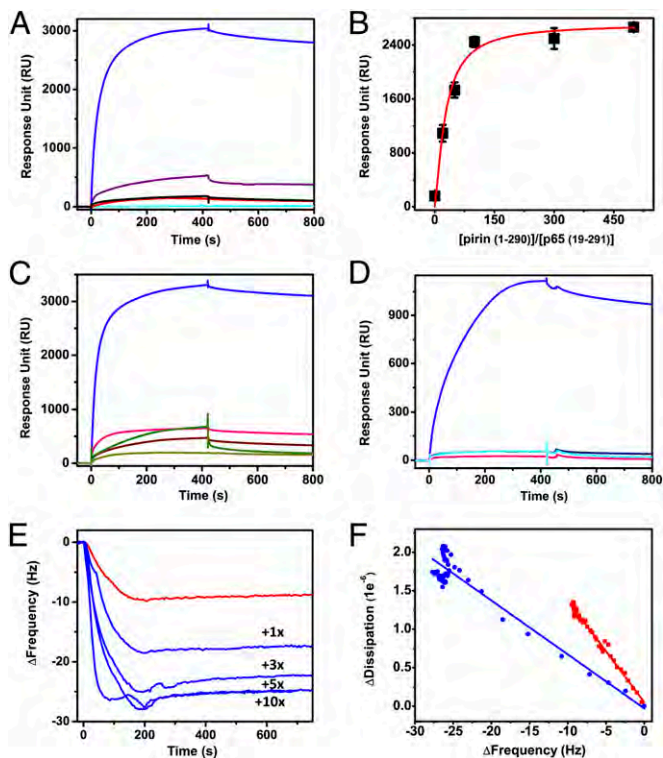


Fig. 1. The ferric, not ferrous, form of pirin substantially facilitates binding of p65 to the I κ B gene in SPR spectroscopy. (A) Detection of apo-, Fe(II)-, and Fe(III)-pirin effects on p65 binding to the I κ B site. (B) Response unit as a function of the pirin (1–290):p65 (19–291) ratio. (C) SPR spectroscopy with Fe(III)- and metal-substituted pirin proteins. (D) Effect of exogenous pirin on native NF- κ B of the nuclear extract of HeLa cells. (E) QCM-D spectroscopy of p65 alone (red trace) and along with Fe(III)-pirin in 1:1–1:10 ratio (indicated by 1 \times , 3 \times , 5 \times , and 10 \times). (F) Comparison of the $\Delta D/\Delta f$ slope in a QCM-D study that indicates a conformational difference of the protein–DNA complex. The SPR traces are color coded with p65 only (red), p65 with Fe(II)-pirin (black), Fe(III)-pirin (blue), metal-stripped pirin (purple), Co(II)-pirin (pink), Mn(II)-pirin (dark yellow), Mn(III)-pirin (wine), and Ni(II)-pirin (olive). Fe(III)-pirin alone (cyan) is shown in A and HeLa nuclear extract only (navy) is shown in D as controls, respectively.

established by performing the same SPR experiment using a nonspecific DNA sequence.

To determine whether other transition metal ions can function in place of the iron cofactor, apo-pirin was prepared from Fe-depleted minimal medium and charged with divalent metal ions. Co-, Mn-, and Ni-reconstituted proteins were stable and contained about 0.6 metal ions per molecule of pirin as determined by inductively coupled plasma optical emission spectrometry (ICP-OES) analysis (Table S1 and *SI Materials and Methods*). These metal-substituted pirin proteins had minimal effects on p65 and were unable to achieve the effect observed for NF- κ B with ferric pirin (Fig. 1C). We wondered whether a metal, other than iron, with correct valence state (i.e., trivalent) would make pirin active. We oxidized Mn(II)-pirin protein, using potassium ferricyanide. After an overnight incubation, the protein was desalted to remove the oxidant and crystallized. As the oxidation state rises, each metal ligand increases its bond length in the Mn-substituted pirin metal center, a scenario similar to what is observed in Fe-pirin structures. The change of the oxidation state of pirin was validated by low-temperature EPR spectroscopy measured before and after the oxidation reaction by the disappearance of the Mn(II) EPR signal. This is the same method we used to generate Fe(III)-pirin from Fe(II)-pirin, with the exception of a shorter incubation time (4 h) after which the colorless Fe(II)-pirin turned into a pale yellow-colored solution and a high-spin ($S = 5/2$) ferric EPR signal

was fully developed from the EPR-silent state. As shown in Fig. 1C, the Co(II)-, Mn(II)-, and Mn(III)-substituted pirin proteins have little or no activity toward NF- κ B. A similar effect was also observed by fluorescence spectroscopy. When the 5'-FAM-labeled κ B DNA was titrated by p65 in the absence of pirin, the 520-nm emission intensity increased as previously reported (27). In contrast, the titration using p65 and Fe(III)-pirin induced an increase in emission signal intensity that was nearly fourfold larger than that using p65 alone, an effect not seen when pirin is complexed with other metals such as Co(II) and Cu(II) (Fig. S1 and *SI Materials and Methods*). The change in fluorescence intensity as a function of p65 concentration resulted in a sigmoidal curve, indicative of the binding cooperativity previously reported in studies of NF- κ B and DNA interactions (27). All of the available reducing agents affect the fluorescein in FAM and resulted in less excitation energy. Thus, the fluorescence assays with Fe(II)-pirin cannot be performed in the current stage.

Pirin's effect on NF- κ B was further investigated with native NF- κ B proteins in cell lines. Fig. 1D shows the effect of isolated pirin on the nuclear extract from HeLa cells, which were not under redox stress; i.e., the NF- κ B proteins were not yet induced for activation. The freshly prepared nuclear extract (at a total protein concentration of 0.08 μ g/mL) was injected into the I κ B-coated SPR sensor chip simultaneously with exogenous Fe(III)-pirin. The inclusion of isolated Fe(III)-pirin protein with the nuclear extract increased binding by about 25-fold compared with that with the extract alone. Fe(II)-pirin and metal-substituted pirin were unable to induce the same effect.

Protein–DNA Supercomplex in the Presence of Pirin Is Compact and Rigid. We also tested whether NF- κ B and the DNA change their structures after forming a complex. Quartz crystal microbalance with dissipation (QCM-D) was used to monitor pirin's effect on

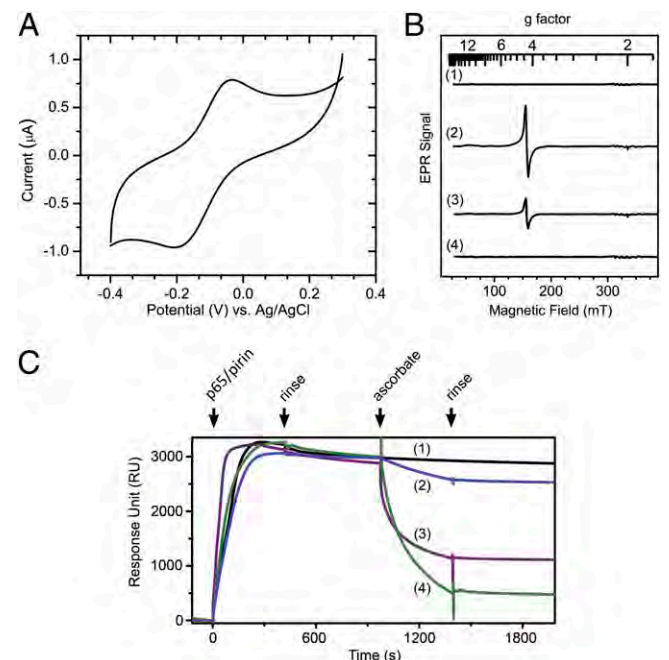


Fig. 2. The function of pirin on p65 is reversible depending on the redox state of the iron center. (A) Determination of the reduction potential of pirin by film cyclic voltammetry in an anaerobic chamber. (B) X-band EPR spectroscopy shows reversibility of the Fe(II)/Fe(III) couple in response to L-ascorbate. Shown are Fe(II)-pirin (250 μ M, trace 1) after oxidation by O $_2$ for 30 min (or 1 equivalent of H $_2$ O $_2$ for 1 min, trace 2) and addition of 1 mM L-ascorbate for 5 min (trace 3) and for 60 min (trace 4). (C) L-ascorbate was introduced to the system, after forming the supercomplex from initial injection of p65/Fe(III)-pirin, at concentrations of 0 (black), 0.25 (navy), 2.5 (magenta), and 25 mM (green) at 980 s.

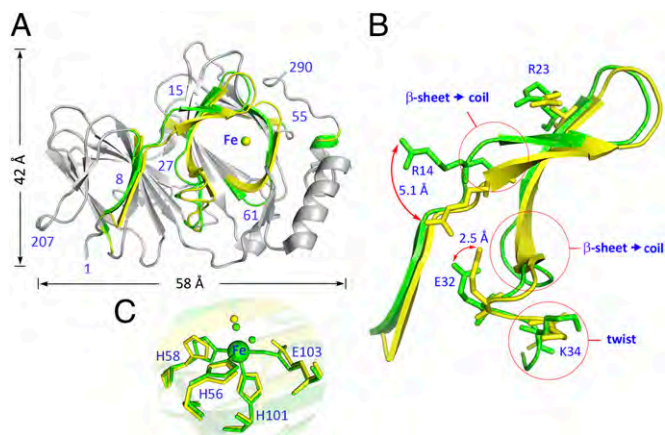


Fig. 3. (A) Structural alignment of ferric (active toward p65) and ferrous (inactive) pirin. Colored regions indicate areas of deviation (≥ 1 Å), whereas gray regions are identical. The structural differences of Fe(III)-pirin are shown in yellow and those of Fe(II)-pirin are in green. (B) The zoom-in view highlights the deviation of a special *R*-shaped area with distinct conformations. (C) Superimposed Fe center structure of ferric (yellow), ferrous (green), and L-ascorbate-reduced (cyan) pirin structures.

the conformation of the p65–DNA complex (Fig. 1E). The plot of the change in dissipation (ΔD) vs. the shift in frequency (Δf) displays a more moderate slope when pirin is present (Fig. 1F). A less steep ΔD vs. Δf slope indicates a more compact, rigid layer formed upon the sensor (28). This result suggests that the conformation of the supercomplex is altered with respect to the NF- κ B and DNA mixture. This observation is also consistent with previous studies showing that κ B sequences are bent to various degrees upon NF- κ B binding (6, 29). DNA bending is a common prerequisite to the formation of a fully active transcriptional complex (30).

Pirin–NF- κ B–DNA Supercomplex Dissociates by Added Reducing Agent.

We determined the midpoint reduction potential (E_m) for the ferrous/ferric couple of pirin by cyclic voltammetry. The resulting curve shown in Fig. 2A resembles published data on the nonheme Fe_B of nitric oxide reductase (31). At pH 7.4, the E_m value is +80 mV vs. an Ag/AgCl electrode. This is 140 mV lower than what was determined for a structurally related protein, Fe-superoxide dismutase (32), which is similarly coordinated by a 3-His-1-carboxylate protein ligand motif. EPR spectroscopic characterization shown in Fig. 2B provides further support that the high-spin ferric ion ($S = 5/2$) in pirin is slowly reduced by L-ascorbate (+58 mV) in a physiologically meaningful context (33). The reduced ferrous ion in pirin is readily oxidized by O₂.

If pirin is indeed a regulatory component in the NF- κ B signaling transduction, it must be able to dissociate after the redox levels resume to normal. We designed a continuous SPR experiment to test whether L-ascorbate would be able to dissociate the pirin•p65•IgkB supercomplex (Fig. 2C). First, the supercomplex was formed and the nonspecifically bound proteins were washed away by buffer. At this point, L-ascorbate was introduced to stimulate a shift in intracellular redox conditions to a less oxidative environment. Fig. 2C shows that L-ascorbate caused the protein supercomplex to dissociate in a dose-dependent manner, and buffer wash without the L-ascorbate immediately halted the dissociation.

Redox State of the Fe in Pirin Affects the Conformation of a Specific *R*-Shaped Surface Area As Revealed by X-Ray Protein Crystallography.

To further our understanding of the structural impact of pirin metal center, especially the differences between the active Fe(III)- and inactive Fe(II)-pirin and the metal-substituted pirin variants, we determined multiple X-ray crystal structures of the active form of Fe(III)-pirin at 1.80- to 2.50-Å resolutions (Table S2). All of the pirin crystals, including ones we analyzed and previously published

(19), belong to the $P2_12_12_1$ space group with one molecule per asymmetric unit.

An apparent structural change is observed when the active ferric form of pirin is aligned with the inactive resting state of ferrous pirin. Fig. 3A shows that the deviations are primarily located on one face of the protein. The residues involved collectively account for *ca.* 20% of 290 total residues. Notable in our structural study, a specific, *R*-shaped surface loop area is identified that is substantially altered due to switching of the metal oxidation state. This area consists of residues 7–41 and 53–62, which includes the surface area surrounding the metal-binding cavity at the N terminus as well as the interface between the two cupin domains. Although the root-mean-square deviation (rmsd) of shift in the protein backbone of this *R*-shaped region between the Fe(II) and Fe(III) states is modest, the widespread coverage and especially the cumulative effect of the changes in the amino acid residues are extensive for a protein of this size. Both sheet-to-coil transition and twist of orientations are observed in the *R*-shaped region. Four charged residues (Arg14, Arg23, Glu32, and Lys34) in the *R*-shaped region show two distinct conformations, depending on the oxidation state of Fe (Fig. 3B). Arg14, for example, shifts 5.1 Å when comparing the two structures (Fig. S2).

The structural data also provide clues for the cause of the extensive conformational changes. His56, His58, His101, and Glu103 are the coordination ligands at 2.1, 2.1, 2.3, and 2.3 Å distance from the Fe(II) ion, respectively. Whereas the histidine residues remain coordinated to the Fe ion at 2.1, 2.1, and 2.2 Å, the negatively charged ligand, Glu103, moves away from the Fe ion in the oxidized protein (Fig. 3C). The Fe–Glu103 distance lies in 2.5–3.2 Å in multiple ferric pirin structures determined (Fig. S3). The variation may be caused by metal reduction during data collections at 100 K. Even though the overall protein structure still maintains at the oxidized state, the metal ligand distances may vary. Nonetheless, this is an unexpected observation and the positively charged Fe ion still sits in a highly negatively charged cavity. We noticed that Glu103 connects the *R*-shaped surface through a well-defined H-bond network (Fig. S4). It is highly possible that redox state change-induced *R*-shape loop deviations are mainly triggered by the iron ion through Glu103.

Metal Identity Affects the Conformation of the *R*-Shaped Surface Area.

To understand the structural basis for the functional incapability of metal-substituted pirin proteins, we solved the X-ray crystal structures of Co- and Mn-substituted pirin (Fig. 4 and Table S3). A similar *R*-shaped conformational difference is observed when comparing the active form of ferric pirin with functionally inactive pirin variants charged with Co(II) and Mn(II) (Fig. S5). The changes in the *R*-shaped region are different from one transition metal to the next, but the location and direction of the conformation changes show the same general trend. To understand why oxidized Mn-pirin is not active, which has an oxidation state of +3, we determined its crystal structure. The structure of Mn(III)-pirin (at 2.15 Å resolution) indeed differs from that of Fe(III)-pirin, but the conformation differences are not the same as those for Mn(II)-pirin (1.56 Å resolution).



Fig. 4. (A–C) Structural differences shown in the alignment of ferric pirin (yellow) (A) with Co(II)-substituted pirin (pink), (B) with Mn(II)-pirin (red), and (C) with Mn(III)-pirin (blue). Colored regions indicate areas of deviation (≥ 1 Å), and gray regions indicate identical structural features.

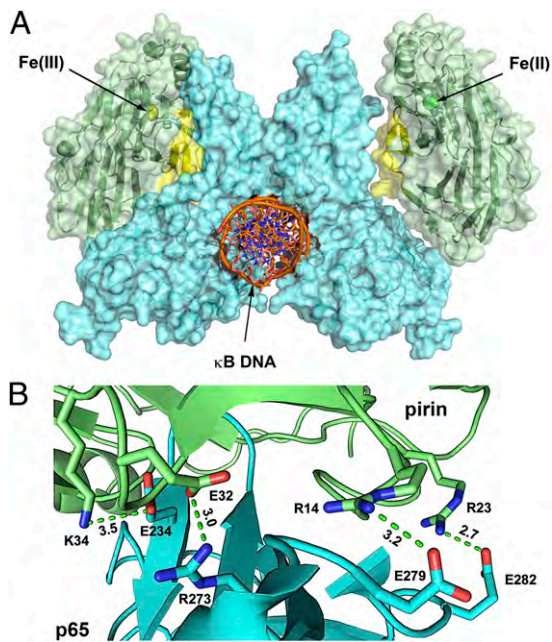


Fig. 5. (A) In silico docking model of pirin (green/yellow)-p65 (blue)-I κ B (golden/blue) supercomplex built from the corresponding crystal structures (*Materials and Methods*). The R-shaped region is highlighted in yellow and the Fe ion is represented in the sphere (ferric in yellow and ferrous in light green). (B) Zoomed-in view of the pirin (upper, green)-p65 (lower, cyan) interface region shows multiple complementary ion-pair interactions, including K34-E234, E32-R273, R14-E279, and R23-E282 (pirin-p65).

R-Shaped Region on Pirin Interacts with the C-Terminal Domain of NF- κ B Proteins. The structural data led us to hypothesize that the R-shaped region is the key protein surface in pirin that directly interacts with p65. A docking model study was subsequently conducted using ZDOCK (34) to further investigate how pirin makes contacts with p65 (26). The result suggests that the R-shaped surface region is the pirin-p65 interface (Fig. 5A). The R-shaped region forms much of the central binding surface between the two proteins (Fig. 5B). The binding takes place at the C-terminal Rel homology domain. The most interesting finding from the docking study is the presence of four ion pairs interacting between pirin and p65. The R-shaped surface residues Arg14, Arg23, Glu32, and Lys34 of ferric pirin are electrostatically complemented by p65 residues Glu279, Glu282, Arg273, and Glu234 at distances of 3.2, 2.7, 3.0, and 3.5 Å, respectively, forming four ion pairs (Fig. 5B). Interestingly, these four residues contribute to the major changes of the R-shaped region as shown in Fig. 3. In contrast, these ion pair interactions are missing when the Fe(II)-pirin structure is used for docking.

The R-shaped region was tested by site-directed mutagenesis. R23E, E32V, K34V, and double-mutant S13R/R14W of the R-shaped region mutants were generated and analyzed. These pirin variants were reconstituted with Fe(II) and oxidized before SPR analysis in the same manner as for the wild-type protein. Fig. 6A shows that these mutations have a significant adverse effect on the binding of pirin to p65 compared with the wild-type protein, reducing the binding efficiency to one- to two-thirds of the wild type. Although there was less DNA binding in these mutants, the resulting supercomplex was still tightly bound and showed a similar lack of dissociation to that of the wild type. Q115N pirin was generated and used as a control along with wild-type pirin. Q115 is not part of the R-shaped region. It is located in the interior of the protein. Not surprisingly, Q115N essentially behaved the same as wild-type pirin. These results demonstrate that site-directed mutation of the surface loop residues dramatically changes the ability of pirin to facilitate p65 binding to the κ B site and thereby supports the docking model.

A 1.70-Å resolution crystal structure of the E32V mutant was obtained in its oxidized form (4HLT, Table S4). The structure shows that mutation of Glu32 disrupts the electrostatic interaction between Glu32 and Arg14 (Fig. 6B). The two residues are within 3.2 Å in the ferric form of native pirin, but Val32 and Arg14 are 9.4 Å apart in E32V. Consequently, the position of the guanidinium group of Arg23 is also shifted. Among the four charged residues, Lys34 is the only residue that is nearly not affected by mutation. This structure provides a molecular rationale for the negative impact of the mutation. Together, these data validate the R-shaped region as the functionally important area of pirin for interaction with p65.

Discussion

On the basis of previous work and this study, it is concluded that human pirin is a redox sensor in the cell nucleus that functions as a coregulator of NF- κ B. Fig. 7 presents an iron-dependent bioinorganic scheme for how NF- κ B could respond to redox changes within the nucleus. Previous studies have established that NF- κ B activation is first achieved by phosphorylation of the inhibitory I κ B proteins in the cytoplasm to liberate NF- κ B. Upon translocation of NF- κ B to the nucleus, several layers of activation take place, involving different coregulators and mechanisms. In the nucleus, under normal reducing conditions, pirin resides in its inactive ferrous state. The results presented here show that, when the redox environment shifts to more oxidizing conditions, pirin responds by changing to its functionally active ferric form and turns on the transcription factor. This is a reversible redox process, depending on the oxidation state of the iron. The dependence of pirin on its iron cofactor is likely an additional contributing factor to the link between iron and NF- κ B in the nucleus.

It remains to be determined whether the proposed nonheme iron protein-based redox switch operates in vivo. However, our findings are consistent with recent biological studies showing increased expression of pirin in response to oxidative stress (24, 35, 36). Interestingly, pirin-like proteins in plants and prokaryotes have also been linked to stress-induced responses and programmed cell death (37). Up-regulation of pirin expression by chronic cigarette smoking has been associated with bronchial epithelial cell apoptosis, presumably due to increased oxidative stress that triggers Nrf2-modulated genes including pirin (35). The conclusion that the oxidation state and activity of pirin is regulated by cellular redox conditions is consistent with those previous findings proposing a role as a protector against oxidative stress. Thus, oxidative stress elevates both the expression of pirin and its activity. When redox levels are restored to normal reducing conditions in the cell nucleus, the transcriptional response induced by pirin may be ablated by reducing its expression and by losing its ability to form a complex with NF- κ B and DNA. However, the present work does not exclude the possibility that there is another

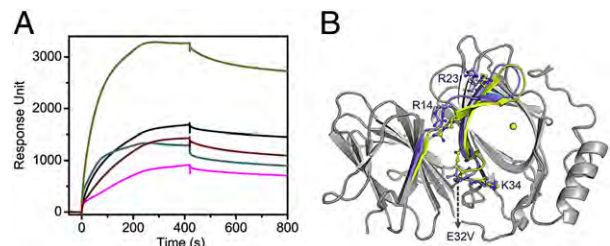


Fig. 6. Mutation at the R-shaped surface impairs the ability of pirin to enhance the DNA-binding ability of p65 to the I κ B site. (A) SPR assay using p65 and immobilized I κ B with R23E (black trace), E32V (cyan), K34V (wine), and S13R/R14W (magenta). The nonsurface mutant Q115N (dark yellow) was used as a positive control. (B) Crystal structure of E32V aligned with native pirin structure. Colored regions indicate areas of deviation (≥ 1 Å), and gray regions indicate identical structural features.

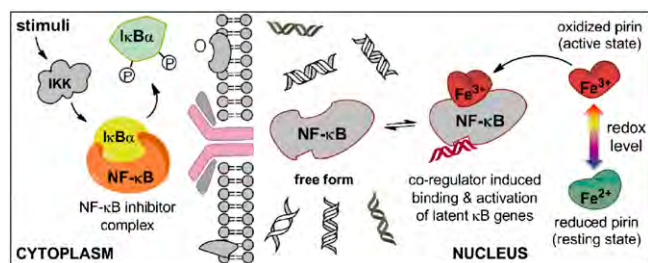


Fig. 7. Proposed function of human pirin. This model depicts a nonheme iron- and oxidation state-dependent regulation mechanism of NF- κ B in the cell nucleus.

protein responsible for oxidizing pirin in the nucleus as a part of a signaling cascade.

Pirin has been proposed to be an important factor in cell differentiation (38). In progenitor cells, the activation of pirin is an important event that alters the transcription profile of the cell to one that primes the cell for differentiation (38). Reduced pirin expression is a common feature of acute myelogenous leukemia, which results in the proliferation of immature myeloid cells. Elevation in the concentration of reactive oxygen species (ROS) has been reported to facilitate differentiation in hematopoietic progenitor cells (39).

Pirin uses a structure-based conformational switch to quickly, reversibly, and efficiently inform the transcription factor of the positive/negative shift of redox levels in the nucleus. The data presented here suggest that the Fe center in pirin is not its active site. Instead, the role of the Fe center is allosteric control. The R-shaped surface loop region is the site that interacts with p65. The two distinct conformational states on the R-shaped surface loop regions endow pirin with the ability to regulate NF- κ B with full reversibility. This unique property distinguishes pirin from any other redox regulators of transcription factors, including the H₂O₂ sensor PerR found in a bacterial source (40). PerR and pirin are both redox sensors with a similar dependence on nonheme iron. Unlike human pirin, PerR itself is a transcription factor. The Fe ion of PerR participates in a Fenton-type reaction with H₂O₂. The result of this reaction is the formation of a hydroxyl radical that irreversibly oxidizes one of its histidine metal-binding ligands, resulting in a drastically altered protein conformation that is no longer able to bind to DNA (40, 41). In contrast, the regulatory mechanism of redox sensing illustrated in Fig. 7 uses a reversible Fe(II)/Fe(III) oxidation state coupling and a consequent reversible conformational switch. The conformational variation of the R-shaped loop areas of pirin can respond accordingly to the oxidation level in the cell nucleus, which allows pirin to respond to redox potential shifts in both directions.

Materials and Methods

Protein Materials. The full-length (1–290 aa) untagged form of human pirin was cloned and expressed in *Escherichia coli* strain BL21(DE3) (Invitrogen). The purification of pirin protein consisted of ammonium sulfate fractionation and three major chromatographic steps including SP Sepharose, Superdex 75, and MonoS on an ÄKTA FPLC system. The metal-free apo-protein of pirin was isolated from iron-depleted minimum medium (42) and metal reconstitution details are given in *SI Materials and Methods*. p65 (19–291) was obtained from Jim Maher, III of Mayo Clinic College of Medicine (Rochester, MN) (43, 44) and isolated as described in the *SI Materials and Methods*. The purified p65 was treated with 10 equivalents of EDTA overnight and then desalted with 20 mM Tris-HCl buffer (pH 7.4) containing 50 mM NaCl and 5% (vol/vol) glycerol.

Metal Analysis. Metal contents of each pirin sample were determined by inductively coupled plasma optical emission spectrometry, using a Spectro Genesis spectrometer (Spectro Analytical Instruments GmbH). Calibration curves were obtained by measuring the standards at the concentrations of each element at 0, 0.1, 0.3, 0.5, 1.0, and 10 ppm (mg/L).

Nuclear Extract Containing Native NF- κ B Proteins. A nuclear extract of HeLa cells was prepared by using the Subcellular Protein Fractionation Kit for Cultured Cells from Pierce Protein Research Products (Thermo Fisher Scientific), according to the manufacturer's protocols. Before injection, the extract was diluted to 0.08 μ g/mL by the SPR binding buffer described above. The binding measurements were taken with the extract alone and together with added pirin (10 μ M) protein.

DNA. The κ B-site DNA used was synthetic oligonucleotide 5'-biotin-GAGTT-GAGGGGACTTCCAGGC-3' (κ B site is shown in boldface type). The single-strand DNA was annealed to its complementary strand before use. A non-specific DNA sequence of 5'-CCTATATGCGCGTATATCC-3' was used as a negative control.

Spectroscopy. SPR measurements were carried out on a Biacore T200 instrument (GE Healthcare). Biotinylated double-stranded Ig κ B DNA was immobilized to streptavidin-coated sensor chips, using standard procedures. The protein–DNA binding was carried out at 20 °C. The effect of pirin upon NF- κ B binding the Ig κ B sequence was studied by flowing the protein over the sensor chip and comparing the levels of DNA binding in the absence and presence of the putative coregulator protein. The final concentration of p65 was 50 nM in the SPR injection buffer whereas pirin concentration was varied from 0 to 25 μ M. After injecting protein samples for 420 s, buffer was injected from 420 to 1,220 s to rinse the weakly bound proteins from the chip surface to monitor the dissociation of the protein or protein complexes. Vitamin C was injected at 980 s in the reversibility testing experiments. The sensor chip surface was regenerated with 0.1% SDS and 3 mM EDTA between each measurement. The anaerobic SPR experiments were performed using O₂-free, argon-saturated buffer.

QCM-D measurements were performed on an E4 instrument (Q-Sense) with biotin-functionalized sensors. Streptavidin was flowed over the biotinylated surface, followed by biotin-labeled Ig κ B-site DNA for immobilization. The equilibrium buffer was 20 mM Tris-HCl (pH 7.4) containing 50 mM NaCl. In each measurement, a total volume of 500 μ L was continuously injected at a flow rate of 150 μ L/min followed by buffer injection for an additional 300 s. The net change in frequency and dissipation was calculated by subtracting the values recorded at the sample injection time from those recorded at the end of each rinsing step. This eliminated the influence of nonspecific, loosely bound proteins on the DNA-immobilized surface. The surface was regenerated between each sample injection by flowing through 0.05% SDS followed by the equilibrium buffer until the baseline was restored. The concentration of p65 was maintained at 0.5 μ M, whereas pirin concentration varied between 0, 0.5, 1.5, 2.5, and 5 μ M for each run of the sample application.

Fluorescence spectroscopy was performed on a Cary Eclipse fluorescence spectrophotometer from Agilent Technologies. Purified p65 was titrated into the fluorescence cuvette containing FAM-labeled double-stranded DNA with Ig κ B sequence in the presence or absence of Fe(III)-pirin or pirin reconstituted with other metal ions in 20 mM Tris-HCl buffer (pH 7.4) and 50 mM NaCl.

The midpoint redox potential of pirin was determined by using a single-wall carbon nanotube-modified electrode in a spectroelectrochemical cell hosted in a N₂-filled, O₂-free plastic bag. Pirin (500 μ M) in 50 mM Tris-HCl (pH 7.4) was used in this study. The formal potential was obtained from the recorded cyclic voltammetry curves.

X-band EPR spectra were obtained in perpendicular mode on a Bruker E200 spectrometer at 100-kHz modulation frequency, using a high-sensitivity resonator ER4119HS at 10 K, maintained by an ESR910 liquid helium cryostat and an Oxford ITC503S temperature controller. Pirin (160 μ L per sample, 200–450 μ M) was prepared in a quartz EPR tube with 20 mM Tris-HCl buffer (pH 7.4) containing 50 mM NaCl.

Crystallization and X-Ray Structure Determination. Pirin was crystallized through optimization of the conditions previously established (19) by hanging-drop vapor diffusion in VDX plates (Hampton Research). Single crystals suitable for X-ray data collection were obtained from drops assembled with 1 μ L protein solution layered with 1 μ L reservoir solution containing 0.1 M MOPS buffer (pH 6.5), 15% PEG 20,000. Crystal growth took place in a vibration-free crystal growth refrigerator from Molecular Dimensions at 16 °C. The crystals were mounted in small loops of fine rayon fiber and flash-cooled directly in liquid nitrogen after being dipped into the cryoprotectant solution that contained 0.1 M MOPS (pH 6.5), 17% PEG 20,000 and 30% ethylene glycol. Initial screening was carried out using a Rigaku MicroMax 007 HF Cu-rotating anode X-ray generator, operated at 40 V and 30 mA, and using a Saturn 944 CCD area detector at Emory University (Atlanta). X-ray diffraction data of Fe(III)-pirin, putative Fe(II)-bound

peroxo pirin, Mn(III)-pirin, and Co(II)-pirin were collected by the Rigaku X-ray facility. X-ray diffraction data of Mn(II)-pirin were collected at the Southeast Regional Collaborative Access Team (SER-CAT) beamline 22-ID at the Advanced Photon Source (APS), Argonne National Laboratory, Argonne, IL. All data collection was performed at 100 K. The diffraction data were processed and analyzed as described in the *SI Materials and Methods*.

In Silico Docking of the Supercomplex. The docking model of pirin with p65 and κ B DNA was constructed by using the ZDOCK utility and server (<http://zdock.umassmed.edu>) (34). The PDB files of ferric pirin (PDB ID: 4GUL) and p65 (PDB ID: 1RAM) (26) were used in model building. The top-ranked result shown in Fig. 5 involves the R-shaped area of pirin, which has been shown in the structural study to differ in conformation when the metal oxidation state changes or metal substitution occurs.

Experimental Validation of the Docking Study. The modeling results were further tested by site-directed mutagenesis experiments. The point mutants of pirin were generated by using the QuikChange II kit purchased from Qiagen (for details, see *SI Materials and Methods*). The sequences of the mutants were verified by DNA sequencing before expressing and purifying proteins. The procedures used for the expression, purification, metal reconstitution, and oxidation of the pirin variants were the same as described previously for the wild-type protein.

- Sen R, Baltimore D (1986) Multiple nuclear factors interact with the immunoglobulin enhancer sequences. *Cell* 46(5):705–716.
- Sen R, Baltimore D (1986) Inducibility of κ immunoglobulin enhancer-binding protein NF- κ B by a posttranslational mechanism. *Cell* 47(6):921–928.
- Romashkova JA, Makarov SS (1999) NF- κ B is a target of AKT in anti-apoptotic PDGF signalling. *Nature* 401(6748):86–90.
- Karin M, Lin A (2002) NF- κ B at the crossroads of life and death. *Nat Immunol* 3(3):221–227.
- Li Q, Verma IM (2002) NF- κ B regulation in the immune system. *Nat Rev Immunol* 2(10):725–734.
- Chen FE, Huang DB, Chen YQ, Ghosh G (1998) Crystal structure of p50/p65 heterodimer of transcription factor NF- κ B bound to DNA. *Nature* 391(6665):410–413.
- Ghosh S, May MJ, Kopp EB (1998) NF- κ B and Rel proteins: Evolutionarily conserved mediators of immune responses. *Annu Rev Immunol* 16:225–260.
- Ghosh G, van Duyn G, Ghosh S, Sigler PB (1995) Structure of NF- κ B p50 homodimer bound to a κ B site. *Nature* 373(6512):303–310.
- Pahl HL (1999) Activators and target genes of Rel/NF- κ B transcription factors. *Oncogene* 18(49):6853–6866.
- Gilmore TD (2008) NF- κ B target genes. Available at <http://www.bu.edu/nf-kb/gene-resources/target-genes/>.
- Gosselin K (2004) NF- κ B target genes. Available at <http://bioinfo.lifl.fr/NF-KB/>.
- Jeong KW, et al. (2011) Recognition of enhancer element-specific histone methylation by TIP60 in transcriptional activation. *Nat Struct Mol Biol* 18(12):1358–1365.
- Merson TD, et al. (2006) The transcriptional coactivator Querkopf controls adult neurogenesis. *J Neurosci* 26(44):11359–11370.
- Näär AM, Lemon BD, Tjian R (2001) Transcriptional coactivator complexes. *Annu Rev Biochem* 70:475–501.
- Oeckinghaus A, Hayden MS, Ghosh S (2011) Crosstalk in NF- κ B signaling pathways. *Nat Immunol* 12(8):695–708.
- Chen FE, Ghosh G (1999) Regulation of DNA binding by Rel/NF- κ B transcription factors: Structural views. *Oncogene* 18(49):6845–6852.
- Wendler WMF, Kremmer E, Förster R, Winnacker E-L (1997) Identification of pirin, a novel highly conserved nuclear protein. *J Biol Chem* 272(13):8482–8489.
- Dechend R, et al. (1999) The Bcl-3 oncoprotein acts as a bridging factor between NF- κ B/Rel and nuclear co-regulators. *Oncogene* 18(22):3316–3323.
- Pang H, et al. (2004) Crystal structure of human pirin: An iron-binding nuclear protein and transcription cofactor. *J Biol Chem* 279(2):1491–1498.
- Gurmu D, et al. (2009) The crystal structure of the protein YhaK from *Escherichia coli* reveals a new subclass of redox sensitive enterobacterial bicupins. *Proteins* 74(1):18–31.
- Adams M, Jia Z (2005) Structural and biochemical analysis reveal pirins to possess quercetinase activity. *J Biol Chem* 280(31):28675–28682.
- Licciulli S, et al. (2011) Pirin inhibits cellular senescence in melanocytic cells. *Am J Pathol* 178(5):2397–2406.
- Miyazaki I, Simizu S, Okumura H, Takagi S, Osada H (2010) A small-molecule inhibitor shows that pirin regulates migration of melanoma cells. *Nat Chem Biol* 6(9):667–673.
- Brzóska K, Stepkowski TM, Kruszewski M (2011) Putative proto-oncogene Pir expression is significantly up-regulated in the spleen and kidney of cytosolic superoxide dismutase-deficient mice. *Redox Rep* 16(3):129–133.

Accession Code. Atomic coordinates and structure factors have been deposited with the Protein Data Bank under accession codes (resolution) 4GUL (1.80 Å), 4EWA (2.47 Å), 4EWE (1.56 Å), 4ERO (2.65 Å), 4EWD (2.15 Å), and 4HLT (1.70 Å).

ACKNOWLEDGMENTS. We thank Michael Hebert and Howard Xu for assistance in pirin cloning, Jim Maher for providing us with a plasmid of p65, Jonathan Hosler for metal content analyses, W. David Wilson for helping us with SPR data acquisition and for providing us with a non-specific DNA sequence, Binghe Wang for providing access to QCM-D instrumentation, Zhi-Ren Liu for providing the HeLa cells, Hiroshi Tachikawa for electrochemical experiments, and Xiaodong Chen for allowing access to the Saturn 944 X-ray facility through a fee-based contract. X-ray data were collected at Emory University and the Southeast Regional Collaborative Access Team (SER-CAT) 22-ID beamline at the Advanced Photon Source, Argonne National Laboratory. We thank Bi-Cheng Wang and the SER-CAT staff as well as John Horton for assistance of X-ray data collections. Use of the Advanced Photon Source was supported by the US Department of Energy, Office of Science, Office of Basic Energy Sciences, under Contract W-31-109-Eng-38. We are grateful to John D. Lipscomb for helpful discussions. This work was supported in part by the Georgia Cancer Coalition Distinguished Cancer Scholar Program (A.L.) and National Science Foundation Grant MCB-0843537 (to A.L.). F.L. acknowledges a Georgia State University fellowship administered by the Center for Diagnostics and Therapeutics.

- Gelbman BD, Heguy A, O'Connor TP, Zabner J, Crystal RG (2007) Upregulation of pirin expression by chronic cigarette smoking is associated with bronchial epithelial cell apoptosis. *Respir Res* 8:10.
- Chen YQ, Ghosh S, Ghosh G (1998) A novel DNA recognition mode by the NF- κ B p65 homodimer. *Nat Struct Biol* 5(1):67–73.
- Phelps CB, Sengchanthalangsy LL, Malek S, Ghosh G (2000) Mechanism of κ B DNA binding by Rel/NF- κ B dimers. *J Biol Chem* 275(32):24392–24399.
- Peh WYX, Reimhult E, Teh HF, Thomsen JS, Su X (2007) Understanding ligand binding effects on the conformation of estrogen receptor α -DNA complexes: A combinational quartz crystal microbalance with dissipation and surface plasmon resonance study. *Biophys J* 92(12):4415–4423.
- Schreck R, Zorbas H, Winnacker E-L, Baeuerle PA (1990) The NF- κ B transcription factor induces DNA bending which is modulated by its 65-kD subunit. *Nucleic Acids Res* 18(22):6497–6502.
- Horton NC, Perona JJ (2000) Crystallographic snapshots along a protein-induced DNA-binding pathway. *Proc Natl Acad Sci USA* 97(11):5729–5734.
- Cordas CM, Duarte AG, Moura JJ, Moura I (2013) Electrochemical behaviour of bacterial nitric oxide reductase-evidence of low redox potential non-heme Fe_B gives new perspectives on the catalytic mechanism. *Biochim Biophys Acta* 1827(3):233–238.
- Vance CK, Miller AF (1998) A simple proposal that can explain the inactivity of metal-substituted superoxide dismutases. *J Am Chem Soc* 120(3):461–467.
- Fasman GD (1976) *CRC Handbook of Biochemistry and Molecular Biology: Physical Chemical Data* (CRC, Cleveland), 3rd Ed.
- Chen R, Li L, Weng Z (2003) ZDOCK: An initial-stage protein-docking algorithm. *Proteins* 52(1):80–87.
- Hübner RH, et al. (2009) Coordinate control of expression of Nrf2-modulated genes in the human small airway epithelium is highly responsive to cigarette smoking. *Mol Med* 15(7–8):203–219.
- Mercer BA, Lemaître V, Powell CA, D'Armiento J (2006) The epithelial cell in lung health and emphysema pathogenesis. *Curr Respir Med Rev* 2(2):101–142.
- Orzaez D, de Jong AJ, Woltering EJ (2001) A tomato homologue of the human protein PIRIN is induced during programmed cell death. *Plant Mol Biol* 46(4):459–468.
- Licciulli S, Cambiaghi V, Scafetta G, Gruszka AM, Alcalay M (2010) Pirin down-regulation is a feature of AML and leads to impairment of terminal myeloid differentiation. *Leukemia* 24(2):429–437.
- Owusu-Ansah E, Banerjee U (2009) Reactive oxygen species prime *Drosophila* haematopoietic progenitors for differentiation. *Nature* 461(7263):537–541.
- Lee J-W, Helmann JD (2006) The PerR transcription factor senses H₂O₂ by metal-catalysed histidine oxidation. *Nature* 440(7082):363–367.
- Traoré DAK, et al. (2009) Structural and functional characterization of 2-oxo-histidine in oxidized PerR protein. *Nat Chem Biol* 5(1):53–59.
- Sjöberg BM, Reichard P, Gråslund A, Ehrenberg A (1978) The tyrosine free radical in ribonucleotide reductase from *Escherichia coli*. *J Biol Chem* 253(19):6863–6865.
- Vwurster SE, Maher LJ, 3rd (2008) Selection and characterization of anti-NF- κ B p65 RNA aptamers. *RNA* 14(6):1037–1047.
- Chen YQ, Sengchanthalangsy LL, Hackett A, Ghosh G (2000) NF- κ B p65 (RelA) homodimer uses distinct mechanisms to recognize DNA targets. *Structure* 8(4):419–428.

Supporting Information

Liu et al. 10.1073/pnas.1221743110

SI Materials and Methods

Cloning, Expression, and Purification of Recombinant Human Pirin.

The full-length (1–290 aa) untagged form of human pirin was cloned and expressed in *Escherichia coli* strain BL21(DE3) (Invitrogen). Cells were grown at 37 °C in LB media with 50 µg/mL kanamycin until an OD₆₀₀ around 0.6–0.8 was achieved. Protein expression was induced by 0.4 mM isopropyl-β-D-thiogalactopyranoside. Cells were further grown for 16 h at 28 °C before harvesting by centrifugation at 8,000 × g for 15 min. The cells were resuspended in the lysis buffer (15 mL/g cell pellet), which consisted of 20 mM HEPES (pH 7.5), 150 mM NaCl, 2 mM EDTA, 0.2 mM phenylmethylsulfonyl fluoride, 10 mM β-mercaptoethanol, and 5% glycerol. The cell membrane was broken by an automated Cell Disruptor made by Microfluidics (M-110P) to release proteins. After centrifugation at 27,000 × g for 30 min, the crude extract supernatant was subjected to ammonium sulfate fractionation. The fraction containing the target protein was redissolved in 20 mM MOPS (pH 6.5) buffer and desalted by a HiLoad G-25 column (2.6 × 30 cm). Pirin was purified from the desalted eluate to homogeneity through three subsequent major chromatographic separation steps (Hi-Load 2.6 × 20-cm SP-Sepharose, Hi-Load 1.6 × 60-cm Superdex 75, and Mono S 4.6/100 PE columns, respectively) in the MOPS buffer on an ÄKTA Protein Purifier system.

Preparation of Apo-Pirin. Metal-free (apo-) pirin used in the surface plasmon resonance (SPR) experiment was isolated from an iron-depleted minimum medium (1). The purified protein was treated with 10 equivalents of EDTA overnight and then desalted with 20 mM Tris-HCl buffer (pH 7.4) containing 50 mM NaCl and 5% (vol/vol) glycerol. The isolated protein was confirmed to be metal-free by inductively coupled plasma optical emission spectrometry (ICP-OES).

Metal Ion Reconstituted Pirin. Co(II), Mn(II), and Ni(II) (0.5 mM) were incubated with apo-pirin (0.05 mM) in 20 mM Tris-HCl buffer (pH 7.4) containing 50 mM NaCl. The reconstitution reaction was allowed to proceed, followed by a final desalting step to remove free ions. The Co(II)-, Mn(II)-, and Zn(II)-reconstituted pirin proteins were concentrated to ~1 mM stock solution for further use.

The Fe(II) reconstitution reaction was initially carried out in an anaerobic chamber (COY Laboratory Products). Apo-pirin (0.05 mM) was incubated with 1.2 equivalents of ammonium iron(II) sulfate (i.e., Mohr's salt) in a reaction vial under O₂-free conditions. The reaction vial was sealed with a rubber cap and parafilm before being removed from the chamber. It was placed in an ice bucket overnight with gentle stirring. The reconstituted protein was used without further desalting to minimize potential oxidation.

Preparation of Fe(III)- and Mn(III)-Pirin. The oxidation of Fe(II)-pirin to Fe(III)-pirin was achieved by using an excess of potassium ferricyanide (5:1 ratio). After 4 h of incubation, the protein was desalted to remove the oxidant. Ferric pirin shows a pale yellow color, in contrast to the colorless Fe(II) oxidation state. Likewise, oxidation of Mn(II)-pirin to Mn(III) was achieved similarly with the exception of a longer incubation time (overnight). The change of the oxidation state of pirin was confirmed by low-temperature electronic paramagnetic resonance (EPR) spectroscopy measured before and after the oxidation reaction.

Site-Directed Mutagenesis of Pirin. The point mutants of pirin were generated by using the QuikChange II kit (Qiagen). The forward

primer sequences used for site-directed mutagenesis were as follows (mutation sites are underlined):

R23E:	5'-GAAGGGTTGGAGCGGAGTCCGGAGAAGCATT-3'
E32V:	5'-AGCATTGGCAGACCCGTGTTAAAAAATCTGGAT-3'
K34V:	5'-GGCAGACCCGAGTTAGTGAATCTGGATCCGTTT-3'
Q115N:	5'-CATGGCCTAAACCTGTGGGT-3'
S13R/R14W:	5'-AGTGCTCAGGTGGGAGCAGTC-3'

The sequences of the mutants were verified by DNA sequencing before expressing and purifying proteins. The procedures used for the expression, purification, metal reconstitution, and oxidation of the pirin variants were the same as described previously for the wild-type protein.

Preparation of p65. The expression system of His-tagged human p65 (70 kDa, 21–325 aa) was kindly provided by Jim Maher (Mayo Clinic College of Medicine, Rochester, MN). p65 was expressed in *E. coli* strain BL21 and purified on an ÄKTA Protein Purifier system (GE Healthcare) according to previously published procedures with minor modifications, including using Cell Disruptor (Microfluidics; M-110P) for breaking the cell membrane and high-capacity and high-resolution resins in subsequent chromatographic separation steps (2, 3).

DNA Preparation. The κB-site DNA used in the SPR experiments was oligonucleotide 5'-biotin-GAGTTGAGGGGACTTTCCCA-GGC-3' [the nuclear factor κB (NF-κB) binding site is highlighted in boldface type]. These sequence-specific oligonucleotides and their respective complementary counterparts were synthesized by Integrated DNA Technologies. The single-strand DNA was annealed to its complementary strand before use.

SPR Measurement with Isolated Proteins. Biotinylated IκB-site DNA was immobilized to streptavidin-coated sensor chips, using standard procedures, and sensorgrams were generated using a Biacore T200 (GE Healthcare). The protein-DNA binding was carried out at 20 °C in 20 mM Tris-HCl (pH 7.4), containing 50 mM NaCl and 0.005% surfactant P20 (GE Healthcare) at a 50 µL/min flow rate. Each sensor chip contained four channels, the first and third of which were reference channels that did not contain immobilized DNA, and they were used for a blank baseline reading that was subtracted from each measurement presented in the sensorgrams (channel 2 – 1 and channel 4 – 3, respectively). The second channel was used to study protein binding to IκB-site DNA and the last channel was an additional control by which a nonspecific DNA sequence of 5'-CCTATATGCGGCGTATATCC-3' was immobilized (1,000 response unit, about 1 ng/mm² of protein or DNA) (4).

The effect of pirin upon NF-κB binding to the IκB sequence was studied by flowing the protein over the sensor chip and comparing the levels of DNA binding in the absence and presence of the putative coregulator protein. The final concentration of p65 and p50 was 50 nM in the SPR injection buffer while pirin's concentration was varied from 0 to 25 µM. In the p50 experiment, B-cell lymphoma 3-encoded protein Bcl-3 was included at a concentration of 25 nM. After injecting protein samples for 420 s, buffer was injected from 420 to 1,220 s to rinse the weakly bound proteins from the chip surface to monitor the dissociation of the protein or protein complexes. Vitamin C was injected at 980 s in the reversibility testing experiments. The sensor chip

surface was regenerated with 0.1% SDS and 3 mM EDTA between each measurement.

SPR Measurements Under Anaerobic Conditions. To perform anaerobic Biacore experiments involving the aforementioned Fe(II)-pirin, the SPR system was primed with O₂-free, argon-saturated 20 mM Tris-HCl buffer (pH 7.4) containing 50 mM NaCl and 0.005% surfactant P20 at least four times over 0.5 h. All of the proteins, including Fe(II)-pirin, were pretreated in sealed reaction vials attached to a Schlenk line by 20–30 gentle vacuum/argon cycles with stirring at 4 °C. The SPR experiments were conducted with the argon-saturated buffer at 20 °C.

SPR Measurements with HeLa Cell-Free Nuclear Extract. Nuclear extract of HeLa cells was prepared by using the subcellular protein fractionation kit for cultured cells from Pierce Protein Research Products (division of Thermo Fisher Scientific), according to the manufacturer's protocols. Before injection, the extract was diluted to 0.08 µg/mL by the SPR binding buffer described above. The binding measurements were taken with the extract alone and together with added pirin (10 µM) protein.

Analysis of the SPR Data. In the absence of pirin, the data of NF-κB binding to the IκB sequence were fitted by the following one-phase exponential association equation [Eq. S1] for calculating the binding rate constant (K_{on}),

$$R(t) = R_{max} \times (1 - \exp(-K_{on} \times t)), \quad [S1]$$

where t represents injection time and R represents response unit.

In the presence of pirin, the binding curve in the sensorgrams exhibited a two-phase association pattern. The data of NF-κB binding were fitted to the following two-phase exponential association equation [Eq. S2] for calculating the binding rate constants (K_{on1} and K_{on2} , respectively):

$$R(t) = R_{max1} \times (1 - \exp(-K_{on1} \times t)) + R_{max2} \times (1 - \exp(-K_{on2} \times t)). \quad [S2]$$

The ferric pirin-induced p65 binding to the immobilized DNA is tight, so much so that virtually no significant dissociation was observed up to 72 h of continuous buffer injection and rinsing.

Quartz Crystal Microbalance-Dissipation Measurement. Biotin-functionalized sensors were purchased from Q-Sense. Streptavidin was flowed over the biotinylated surface, followed by biotin-labeled IκB-site DNA for immobilization. The equilibrium buffer was 20 mM Tris-HCl (pH 7.4) containing 50 mM NaCl. The quartz crystal microbalance-dissipation (QCM-D) experiments were carried out with freshly prepared proteins after both frequency and dissipation baselines were stabilized. Simultaneous measurement at multiple-frequency overtones of the quartz crystal was conducted but only the data obtained with overtone $n = 5$ were taken for representation. For each measurement, a total volume of 500 µL was continuously injected at a flow rate of 150 µL/min followed by buffer injection for an additional 300 s. The net change in frequency and dissipation was calculated by subtracting the values recorded at the sample injection time from those recorded at the end of each rinsing step. This eliminated the influence of nonspecific, loosely bound proteins on the DNA-immobilized surface. The surface was regenerated between each sample injection by flowing through 0.05% SDS, followed by the equilibrium buffer until the baseline was restored. The concentration of p65 was maintained at 0.5 µM, while pirin's concentration varied between 0, 0.5, 1.5, 2.5, and 5 µM for each run of the sample application.

Fluorescence Spectroscopy. The FAM-labeled double-stranded DNA containing the IκB sequence (*DNA Preparation* section)

was added at a final concentration of 20 nM to a fluorescence cuvette with 0.5 mL binding buffer of 20 mM Tris-HCl (pH 7.4) and 50 mM NaCl. Purified p65 was then titrated into the fluorescence cuvette in the presence or absence of Fe(III)-pirin or pirin reconstituted with other metal ions. Each measurement was performed after 10 min of incubation to allow for complete protein-protein and protein-DNA interactions. The fluorescence measurements were performed on a Cary Eclipse fluorescence spectrophotometer (Varian, part of Agilent Technologies) with an excitation wavelength of 490 nm, an emission wavelength of 520 nm, and a slit width of 10 nm.

Electrochemical Study of Pirin by Cyclic Voltammetry. The midpoint redox potential of pirin was determined by using a single-wall carbon nanotube-modified electrode in a spectroelectrochemical cell hosted in a N₂-filled, O₂-free plastic bag. Pirin (500 µM) in 50 mM Tris-HCl (pH 7.4) was used in this study. The formal potential was obtained from the recorded cyclic voltammetry curves and reported in millivolts vs. Ag/AgCl reference.

EPR Spectroscopy. X-band EPR spectra were obtained in perpendicular mode on a Bruker EMX or E200 spectrometer at 100-kHz modulation frequency, using a high-sensitivity resonator ER4119HS. Low temperature (10 K) was maintained with an ITC503S temperature controller, an ESR910 liquid helium cryostat, and an LLT650/13 liquid helium transfer tube (Oxford Instruments). Measurements were conducted by maintaining the frequency of the electromagnetic radiation constant while the magnetic field was swept. Pirin (160 µL/sample, 200–450 µM) was prepared in quartz EPR tube with 20 mM Tris-HCl buffer (pH 7.4) containing 50 mM NaCl.

ICP-OES. Metal contents of each pirin sample were determined by using a Spectro Genesis spectrometer (Spectro Analytical Instruments GmbH). Calibration curves were obtained by measuring the standards at the concentrations of each element at 0, 0.1, 0.3, 0.5, 1.0, and 10 ppm (mg/L).

Crystallizations and X-ray Structure Determinations. Pirin was crystallized through optimization of the conditions previously established (5) by hanging-drop vapor diffusion in VDX plates (Hampton Research). Single crystals suitable for X-ray data collection were obtained from drops assembled with 1 µL protein solution layered with 1 µL reservoir solution containing 0.1 M MOPS (pH 6.5), 15% PEG 20,000. Crystal growth took place in a vibration-free crystal growth refrigerator from Molecular Dimensions at 16 °C. The crystals were mounted in small loops of fine rayon fiber and flash-cooled directly in liquid nitrogen after being dipped into the cryoprotectant solution that contained 0.1 M MOPS (pH 6.5), 17% PEG 20,000, and 30% ethylene glycol. Initial screening was carried out using a Rigaku MicroMax 007 HF Cu-rotating anode X-ray generator, operated at 40 V and 30 mA, and using a Saturn 944 CCD area detector. X-ray diffraction data were collected by either the Rigaku X-ray facility at Emory University or at the Southeast Regional Collaborative Access Team (SER-CAT) beamline 22-ID of the Advanced Photon Source (APS), Argonne National Laboratory, Argonne, IL. All data collection was performed at 100 K. The diffraction data were indexed, integrated, and scaled with HKL2000 (6). The structures were solved by molecular replacement, using the MOLREP program (7) of the CCP4 suite (8) with Fe(II)-pirin structure [Protein Data Bank (PDB) ID: 1J1L] (5) as a search model. Electron density was fitted and refined using Coot (9), REFMAC (10), and PHASER (11). Figures showing crystal structures were drawn with PyMOL (<http://www.pymol.org>).

In Silico Modeling of the Supercomplex. Rigid docking of pirin with p65 was conducted using the ZDOCK utility and server (<http://>

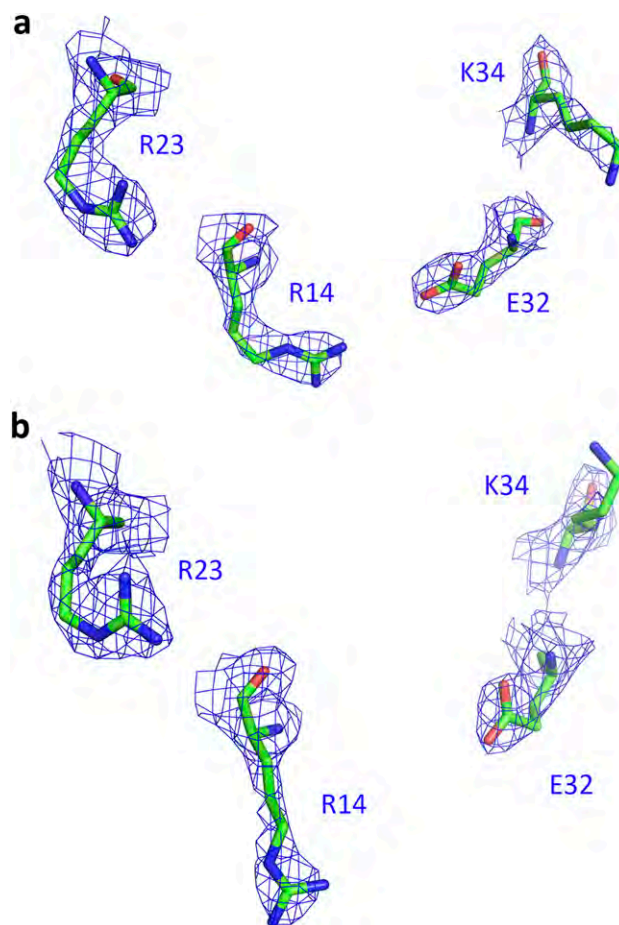


Fig. S2. Key residues in the *R*-shaped surface loop including the relative orientation and the electron densities of Arg14, Arg23, Glu32, and Lys34 in the structural data. (A) Fe(III)-pirin (4GUL). (B) Fe(II)-pirin (1J1L). The $2F_o - F_c$ electron densities are contoured at 1.0σ .

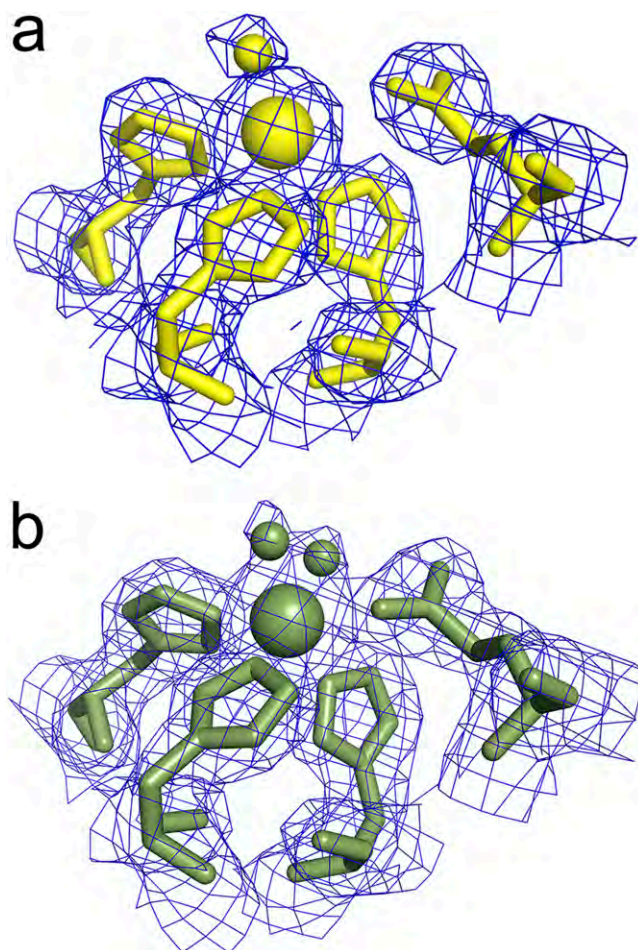


Fig. S3. Electron density comparison of fully oxidized and reduced pirin iron centers. (A) Fe(III)-pirin (4EWA). (B) Fe(II)-pirin (1J1L). The $2F_o - F_c$ electron densities are contoured at 1.0σ . Note that the exact number and the chemical nature (i.e., water or hydroxide) of the solvent-derived ligands cannot be definitely determined by X-ray protein crystallography at these resolutions and they may be affected by the X-ray resource during data collections at 100 K. It should be noted that metal reduction might occur during data collections even with the in-house X-ray facility, consequently causing shifts in the metal ligands and bond distances. Thus, this comparison is intended only for illustrating a trend of changes at the metal center and it should be used with caution.

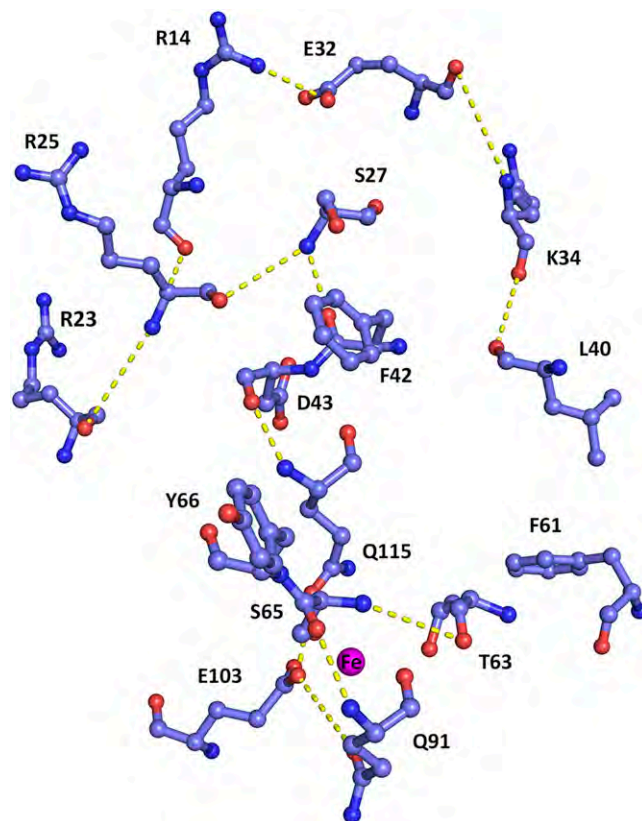


Fig. 54. The Fe center is connected to the pirin “active-site” residues (including Arg14, Arg23, Glu32, and Lys34) through a H-bond network. The metal ligand Glu103 is proposed to trigger conformation changes of the surface residues.

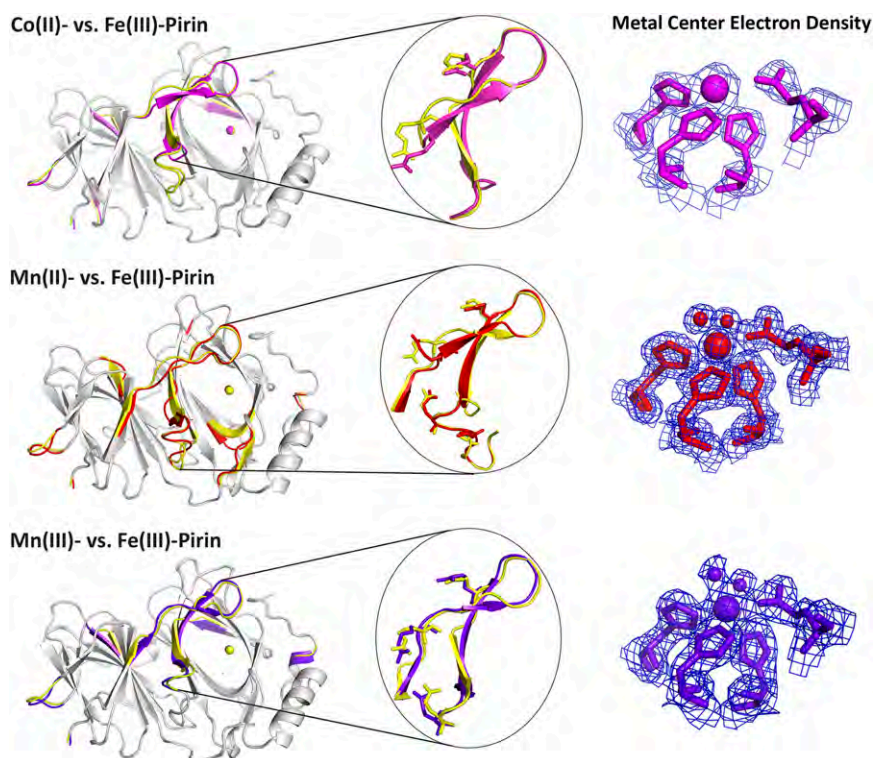


Fig. S5. Structural alignments of Co(II)- (magenta, 4ERO), Mn(II)- (red, 4EWE), and Mn(III)-pirin (purple, 4EWD) against Fe(III)-pirin (yellow, 4EWA). (Right) Metal center electron density maps are shown. The well-aligned parts are shown in gray and in differences in color. The Mn(III) ion is hexacoordinate in the Mn(III)-pirin structure, which is more similar to that of the ferric pirin structure than the Mn(II)- and Co(II)-pirin structures. However, significant difference at the R-shaped region still exhibits, indicating that sole trivalent oxidation state is insufficient for making pirin active and the metal identity is of paramount importance.

Table S1. Metal analysis of pirin by inductively coupled plasma optical emission spectrometry (ICP-OES)

Human pirin protein	Fe	Zn	Cu	Mn	Co	Ni
As-isolated untagged recombinant pirin	0.63	0.19	<0.01	<0.01	<0.01	<0.01
Metal-free apo-pirin	<0.10	<0.01	<0.01	<0.01	<0.01	<0.01
Fe-reconstituted, from apo-pirin	1.00	<0.01	<0.01	<0.01	<0.01	<0.01
Co-reconstituted, from apo-pirin	<0.01	<0.01	<0.01	<0.01	0.60	<0.01
Mn-reconstituted, from apo-pirin	<0.01	<0.01	<0.01	0.63	<0.01	<0.01
Ni-reconstituted, from apo-pirin	<0.01	<0.01	<0.01	<0.01	<0.01	0.61

Preparation of metal-free apo-pirin from a minimum medium and metal ion reconstitution are described in *SI Materials and Methods*. Values were obtained as average of three measurements with SEs less than 5%. The data are presented as molar ratio per pirin molecule.

Table S2. X-ray crystallographic data collection and refinement statistics of human pirin at the active ferric oxidation state

Data collection	Ferric pirin, Synchron	Ferric pirin, in-house facility
Detector type	MAR300 CCD	Saturn 944 CCD
Source	APS, Sector 22-ID	Cu rotating anode
Space group	$P2_12_12_1$	$P2_12_12_1$
Unit cell lengths, Å	$a = 42.30, b = 67.03, c = 107.06$	$a = 42.17, b = 66.70, c = 106.21$
Unit cell angles, °	$\alpha = \beta = \gamma = 90^\circ$	$\alpha = \beta = \gamma = 90^\circ$
Wavelength, Å	0.80	1.54
Temperature, K	100	100
Refinement		
Resolution, Å*	21.88–1.80 (1.85–1.80)	50.00–2.48 (2.52–2.48)
Completeness, %*	99.5 (94.3)	89.5 (75.0)
$R_{\text{merge}}, \%^{*,\dagger}$	14.9 (47.5)	13.1 (52.4)
$\langle I \rangle / \sigma I, ^*$	32.9 (3.6)	21.4 (3.8)
Redundancy*	9.6(3.8)	5.5 (4.7)
Resolution, Å	1.80	2.47
No. reflections, working/test	25,931/1,397	9,419/480
$R_{\text{work}}, \%^\ddagger$	18.7	24.0
$R_{\text{free}}, \%^\S$	23.4	29.6
Ramachandran statistics [¶]		
Preferred, %	96.15	92.66
Allowed, %	2.80	5.94
Bond lengths, Å	0.022	0.006
Bond angles, °	2.258	1.091
PDB access code	4GUL	4EWA
Esu based on R value	0.029	1.752
Esu based on free R value	0.028	0.382

ESU, estimated standard uncertainty.

*Values in parentheses are for the highest-resolution shell.

[†] $R_{\text{merge}} = \sum_i |I_{hkl,i} - \langle I_{hkl} \rangle| / \sum_{hkl} \sum_i I_{hkl,i}$, where $I_{hkl,i}$ is the observed intensity and $\langle I_{hkl} \rangle$ is the average intensity of multiple measurements.

[‡] $R_{\text{work}} = \sum ||F_o| - |F_c|| / \sum |F_o|$, where $|F_o|$ is the observed structure factor amplitude, and $|F_c|$ is the calculated structure factor amplitude.

[§] R_{free} is the R factor based on 5% of the data excluded from refinement.

[¶]Based on values attained from refinement validation options in COOT.

Table S4. X-ray crystallographic data collection and refinement statistics of ferric E32V pirin variant

Data collection	E32V-Pirin
Detector type	MAR300 CCD
Source	APS, Sector 22-ID
Space group	$P2_12_12_1$
Unit cell lengths, Å	$a = 42.41, b = 66.64, c = 107.33$
Unit cell angles, °	$\alpha = \beta = \gamma = 90^\circ$
Wavelength, Å	1.0
Temperature, K	100
Resolution, Å*	31.84–1.70 (1.73–1.70)
Completeness, %*	97.1 (79.8)
$R_{\text{merge}}, \%^{*†}$	7.4 (38.4)
$\langle I \rangle / \sigma I^*$	55.3 (4.0)
Redundancy*	12.2 (6.0)
Refinement	
Resolution, Å	1.70
No. reflections, working/test	31,298/1,677
$R_{\text{work}}, \%^\ddagger$	18.4
$R_{\text{free}}, \%^\S$	23.4
Ramachandran statistics [¶]	
Preferred, %	96.50
Allowed, %	1.75
Root mean square deviation	
Bond lengths, Å	0.023
Bond angles, °	2.353
PDB access code	4HLT
Estimated overall coordinate error	
Esu based on R value	0.110
Esu based on free R value	0.116

*Values in parentheses are for the highest-resolution shell.

[†] $R_{\text{merge}} = \sum_i |I_{\text{hkl},i} - \langle I_{\text{hkl}} \rangle| / \sum_{\text{hkl}} \sum_i I_{\text{hkl},i}$, where $I_{\text{hkl},i}$ is the observed intensity and $\langle I_{\text{hkl}} \rangle$ is the average intensity of multiple measurements.

[‡] $R_{\text{work}} = \sum ||F_o| - |F_c|| / \sum |F_o|$, where $|F_o|$ is the observed structure factor amplitude, and $|F_c|$ is the calculated structure factor amplitude.

[§] R_{free} is the R factor based on 5% of the data excluded from refinement.

[¶]Based on values attained from refinement validation options in COOT.